Electronic Supplementary Information

Experiment Section

Materials: Manganese dichloride tetrahydrate ($MnCl_2 \cdot 4H_2O$), 7,7,8,8-tetracyanoquinodimethane ($C_{12}H_4N_4$), lithium iodide hydrate ($LiI \cdot xH_2O$), and potassium hydroxide (KOH) were purchased from Aladdin Industrial Co.. Acetonitrile (CH_3CN) and isopropyl alcohol (C_3H_8O) obtained from Zhiyuan Chemical Reagent Co.. Nafion solution (5 wt%) was purchased from Sigma-Aldrich. All chemicals were used of analytical grade and used as received without further purification.

Synthesis of Li-TCNQ: $LiI \cdot xH_2O$ (0.2 g) and $C_{12}H_4N_4$ (0.2 g) were dissolved in 40 mL acetonitrile solution and vigorously stirred for 10 min. Then the solution was heated at 60^{o}C for 2 h in water bath. The product was collected by centrifugation, washed with acetonitrile and ethanol, and then dried at 60^{o}C in a vacuum oven.

Synthesis of Mn-TCNQ: Li-TCNQ (0.1 g) and $MnCl_2 \cdot 4H_2O$ (0.2 g) were dissolved in 30 mL acetonitrile solution and vigorously stirred for 10 min. Then the solution was heated at 60^{o}C for 2 h in water bath. The product was collected by centrifugation, washed with acetonitrile and ethanol, and then dried at 60^{o}C in a vacuum oven.

Characterization: The morphologies and microstructures were investigated by scanning electron microscopy (SEM, Quanta FEG 250) and transmission electron microscope (TEM, JEM-2100, JEOL). X-ray diffraction (XRD) pattern was obtained with a XRD-6100 (XRD, Shimadzu XRD-6100) at a scanning rate of 5° min^{-1} from 10° to 80°. The surface properties of the samples were studied by Fourier transform infrared spectroscopy (FTIR, Nicolet 6700, Thermo Scientific) and X-ray photoelectron spectroscopy (XPS, Escalab 250xi, Thermo Scientific). The absorbance data of spectrophotometer was acquired on Ultraviolet-visible (UV-Vis) spectrophotometer (Shimadzu UV-2700).

Electrochemical measurements: 5 mg Mn-TCNQ powder was mixed with 20 uL of 5wt% Nafion solution and ultrasonically dispersed in 0.98 mL isopropyl alcohol solution. Then, 10 μL catalyst ink was loaded onto a pre-polished glassy carbon electrode (D = 5.6 mm) of a rotation ring disk electrode (RRDE) to achieve a catalyst loading ≈ 0.2 mg cm^{-2}. All electrochemical tests were carried on CHI 760E (CHI Instruments Inc.). The RRDE loaded electrocatalyst was used as the working electrode, a platinum foil as counter electrode, and Hg/HgO (saturation KOH) as reference electrode. The electrolyte was 0.1 M KOH solution.

The H_2O_2 selectivity of sample based on RDE was calculated by K-L plot from the polarization curves at different rotation speeds:

$$1/j = 1/j_{\mathrm{kin}} + 1/j_{\mathrm{diff}} = 1/j_{\mathrm{kin}} + 1/(\mathrm{B}\omega^{1/2}) \qquad (1)$$

$$\mathrm{B} = 0.62 \cdot \mathrm{n} \cdot \mathrm{F} \cdot \mathrm{D}_{\mathrm{O}_2}^{2/3} \cdot \nu^{-1/6} \cdot C_{\mathrm{O}_2} \qquad (2)$$

Where j is the current density consists of a kinetic current (j_{kin}) and a diffusion current (j_{diff}), ω is the rotation speed, n is the number of electrons transferred during the reaction, and D_{O_2} and C_{O_2} are the diffusivity and solubility of oxygen, respectively; F is the Faraday constant and v is the kinematic viscosity of the electrolyte. For a $4e^-$ process, B= 0.47 mA cm^{-2} $s^{1/2}$ and for a $2e^-$ process, B = 0.23 mA cm^{-2} $s^{1/2}$.

The linear sweep voltammetry (LSV) curves were tested by RRDE scans from 0 to 1.0 V (vs. RHE) in N_2- and O_2-saturated 0.1 M KOH at a scan rate of 10 mV s^{-1} with a rotation speed of 1600 rpm. During the LSV tests, the Pt ring potential was held at 1.2 V (vs. RHE). The H_2O_2 selectivity was calculated from the RRDE measurement according to following equation:

$$\mathrm{H_2O_2}\ (\%) = 200 \times (\mathrm{I_{Ring}}/\mathrm{N})/(\mathrm{I_{Disk}} + \mathrm{I_{Ring}}/\mathrm{N}) \qquad (3)$$

$$\mathrm{n} = 4\mathrm{I_{Disk}}/(\mathrm{I_{Disk}} + \mathrm{I_{Ring}}/\mathrm{N}) \qquad (4)$$

Where I_{Disk} and I_{Ring} are the measured current of disk electrode and Pt ring electrode, and N is the current collection efficiency of Pt ring (0.37), respectively.

The Faradaic efficiency (FE) is obtained by dividing the amount of charge consumed to synthesize the product by the total amount of charge consumed for the electrode. On the basis that two electrons are needed to generate one H_2O_2 molecule, the FE can be calculated as FE = (2F × c × V)/Q, where *F* is the Faraday constant, *c* is the measured H_2O_2 concentration, *V* is the volume of the electrolyte, *Q* is the total charge used for electrosynthesis.

Electro-generation of H_2O_2: The electro-generation of H_2O_2 was conducted in two-compartment H-type cell. Cathode was prepared by depositing catalyst ink (0.1 mg cm^{-2}) on a carbon paper (CP) (1×1 cm), and platinum foil was used as anode. H_2O_2 yields were measured by using the indicator of $Ce(SO_4)_2$ ($2Ce^{4+} + H_2O_2 \rightarrow 2Ce^{3+} + 2H^+ + O_2$). Samples (30 μL electrolyte) were collected at a certain time (1 h) and mixed with the $Ce(SO_4)_2$ solution (0.1 mmol L^{-1}, 4.97 mL). The mixed solution was detected with UV-vis spectrophotometer. A typical concentration-absorbance curve was calibrated by linear fitting the absorbance values at wavelength length of 318 nm for various standard concentrations of 0.02, 0.04, 0.06, 0.08, 0.1 mM of Ce^{4+}. The fitting curve ($y = 4.3365\ x - 0.00881$, $R^2 = 0.999$) shows good linear relation of absorbance value with Ce^{4+} concentration (Fig. S2). The yields of H_2O_2 were finally determined based on the reduced Ce^{4+} concentration.

The density functional theory (DFT) calculation details: The first principle calculations were performed to reveal the mechanism of ORR on the surface of Mn-TCNQ by using the Vienna ab initio simulation package (VASP).[1,2] The generalized gradient approximation method of Perdew-Burke-Ernzerhof (PBE) functional was used to describe the exchange-related interaction between electrons.[3] The van der Waals (vdW) correction with the Grimme approach (DFT-D2) was included in the interaction between single molecule/atoms and substrates.[4] The energy cutoff for the plane wave-basis expansion was set to 500 eV. The convergence criteria for the total energy and the Hellmann-Feynman force were 10^{-5} eV and 0.02 eVÅ^{-1}, respectively, and adopted a supercell length of 10 Å in the *z* direction. The Brillouin zone was sampled with 3 × 3 × 1 Gamma-center k-point mesh.

The computational hydrogen electrode model has been adopted for calculations of the Gibbs free-energy change for the relevant elemental steps, which can be obtained by $\Delta G = \Delta E + \Delta ZPE - T\Delta S$, where ΔE is the total energy, ΔZPE is the zero point energy and S is the entropy at 298.15 K. The theoretical overpotential (η) of $2e^-$ ORR was deduced using the equation of $\eta = |\Delta G_{*OOH}/e - 4.22\ V|$. The solvation effect was not considered in determining the value of ΔG_{*OOH}, which governs a reasonable comparison.

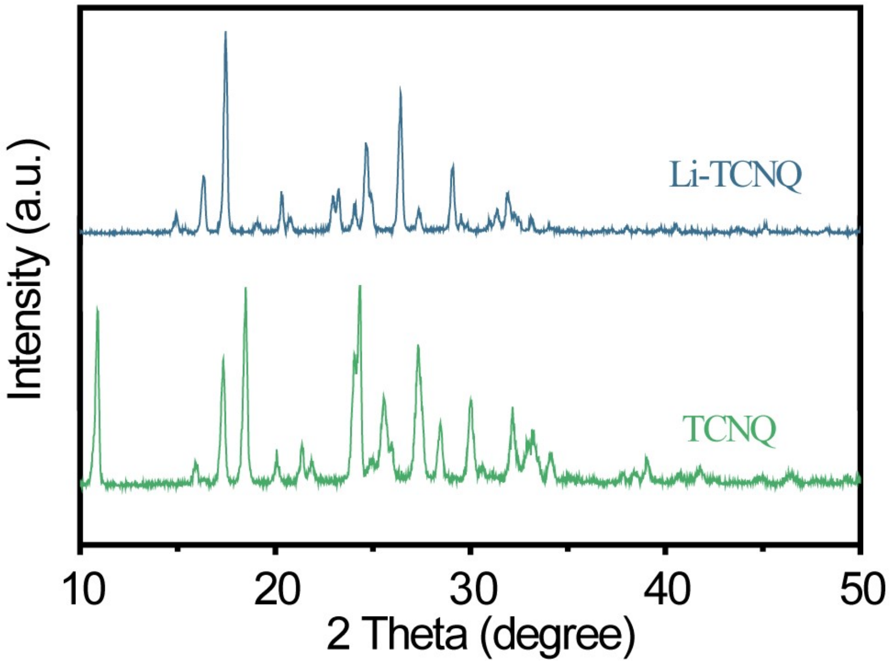

Fig. S1. XRD patterns of TCNQ and Li-TCNQ.

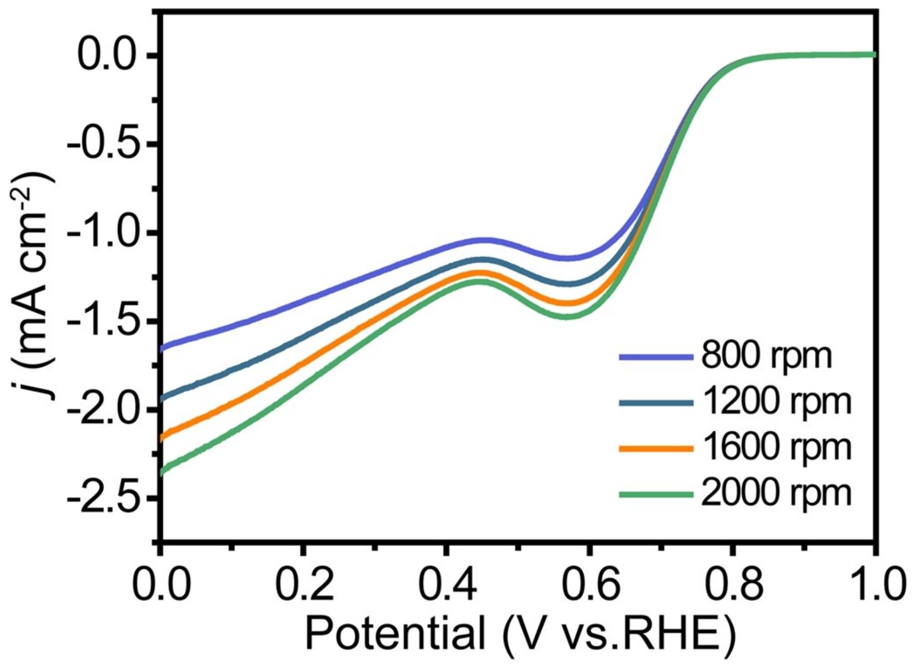

Fig. S2. LSV curves of Mn-TCNQ with different scan rate.

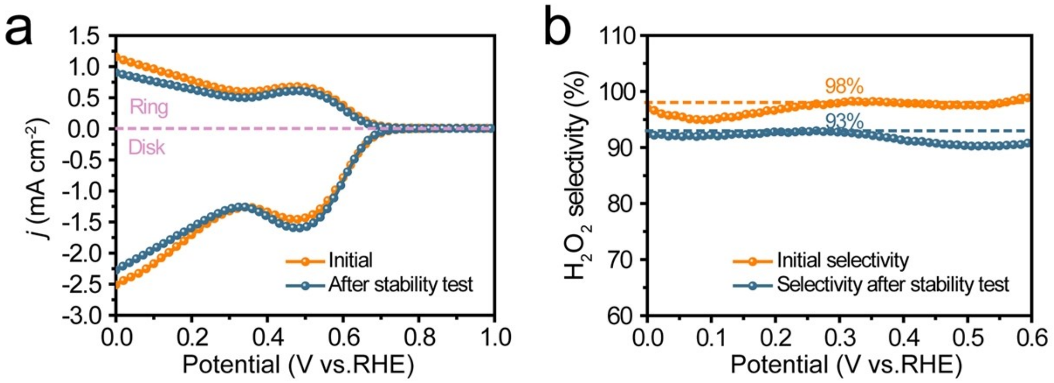

Fig. S3. (a) LSV curves and (b) the H_2O_2 selectivity based on the RRDE measurements before (orange) and after (dark blue) stability test in O_2-saturated 0.1 M KOH electrolyte for Mn-TCNQ.

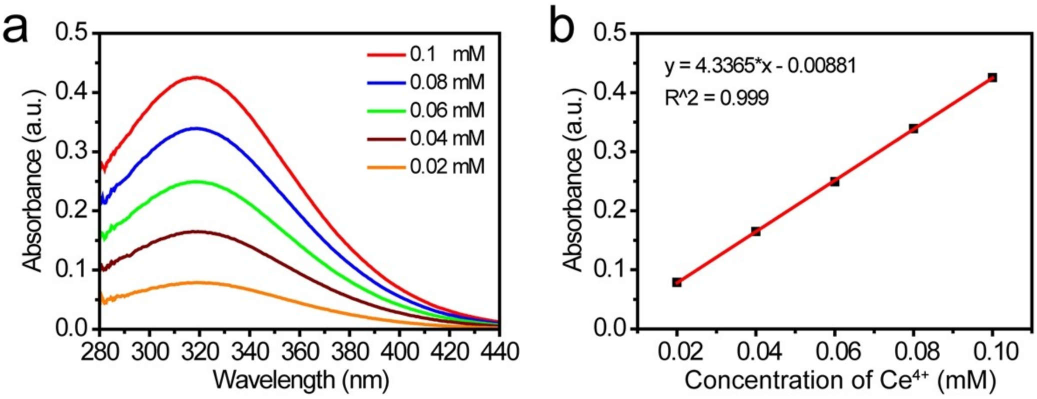

Fig. S4. (a) UV-Vis spectra of Ce^{4+} solution with various concentrations and (b) corresponding standard fitting curve.

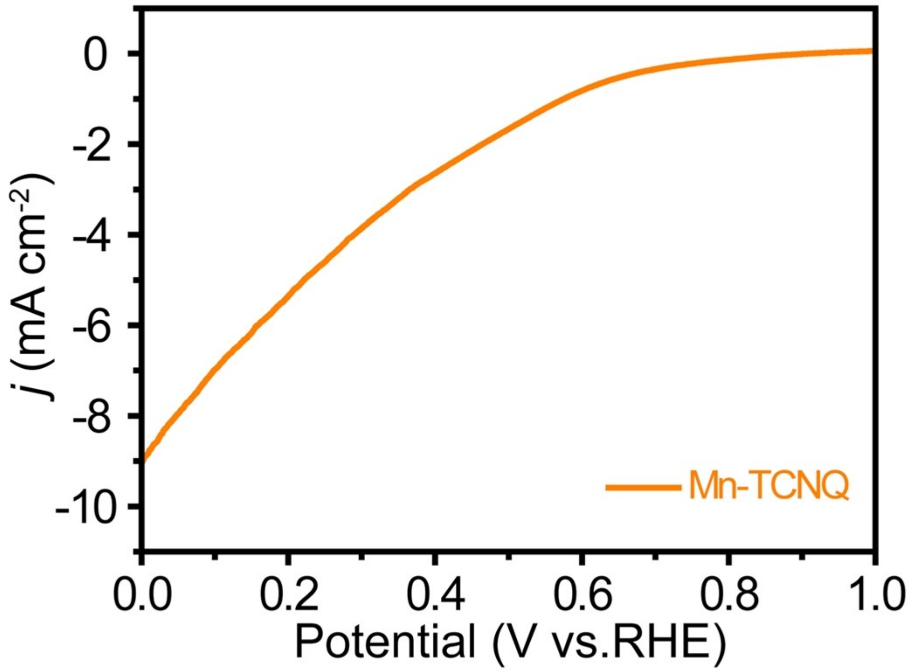

Fig. S5. LSV curve of Mn-TCNQ in O_2-saturated 0.1 M KOH tested using H-type cell.

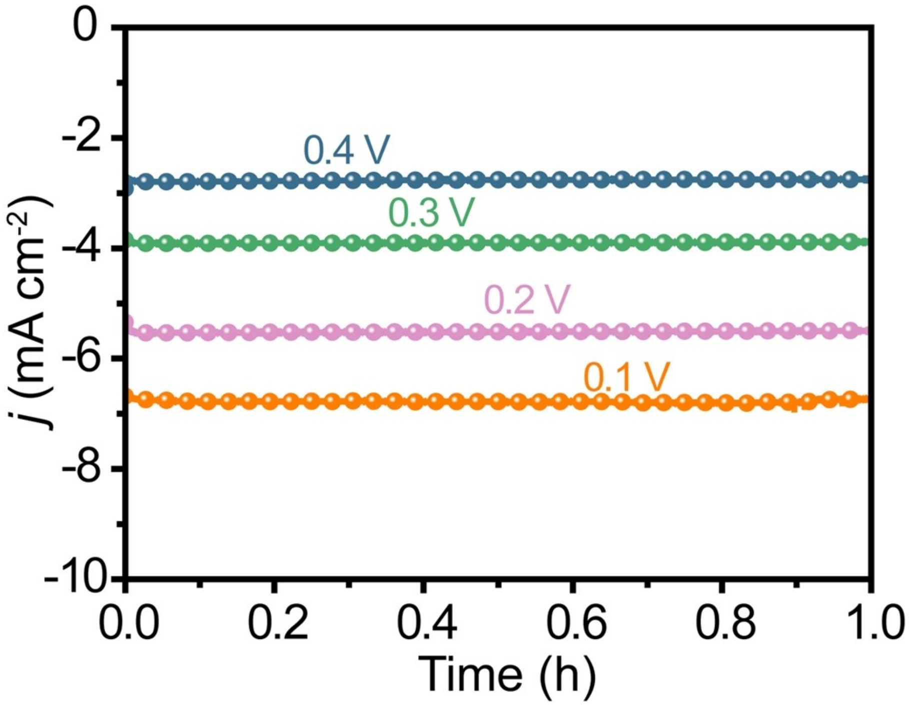

Fig. S6. I-t curves of Mn-TCNQ for 1 h electrolysis in different potentials.

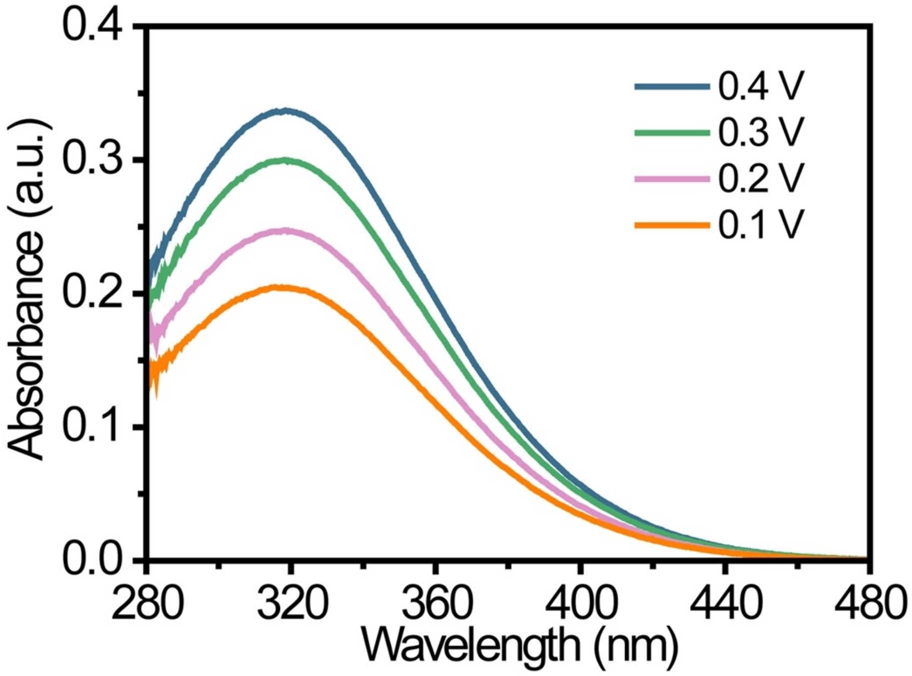

Fig. S7. UV-Vis spectra of electrolyte after1 h electrolysis at various potentials.

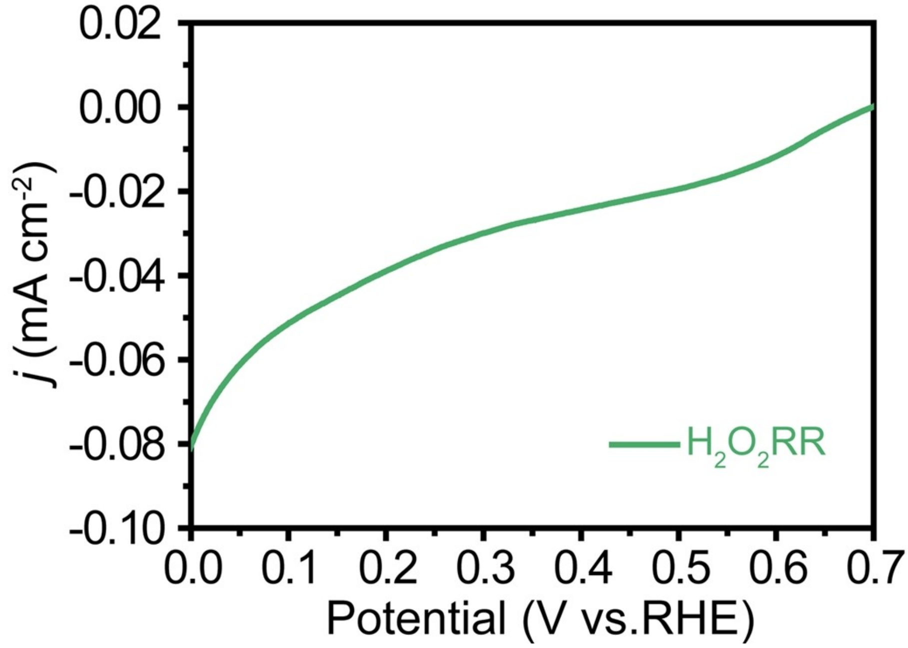

Fig. S8. LSV curve of Mn-TCNQ for H_2O_2RR in N_2-saturated 0.1 M KOH electrolyte containing 10 mM H_2O_2.

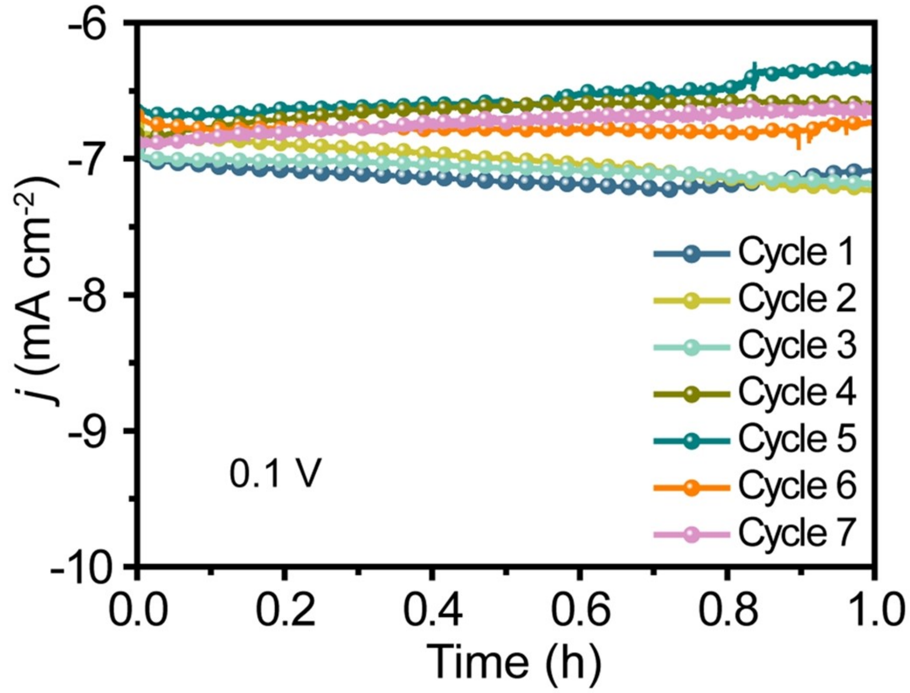

Fig. S9. I-t curves of Mn-TCNQ for 1 h electrolysis with seven cycles at 0.1 V.

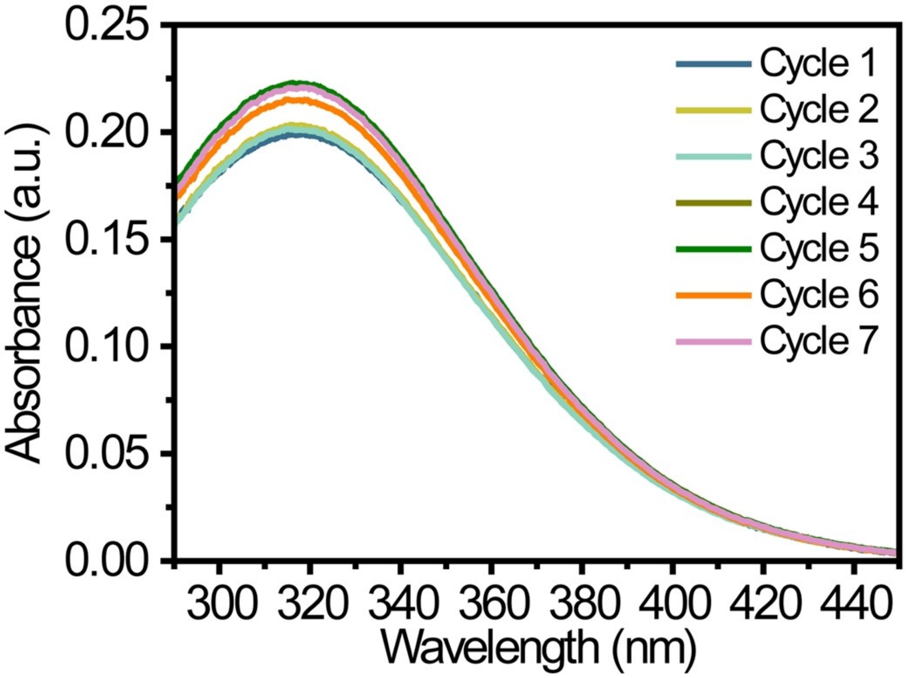

Fig. S10. UV-Vis spectra of seven cycles for electrolyte at 0.1 V.

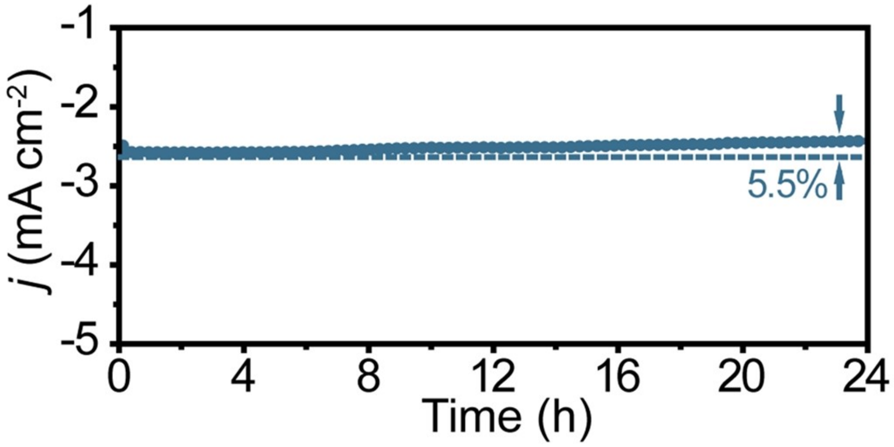

Fig. S11. I-t curve of Mn-TCNQ at 0.4 V in an O_2-saturated 0.1 M KOH for 24 h electrolysis.

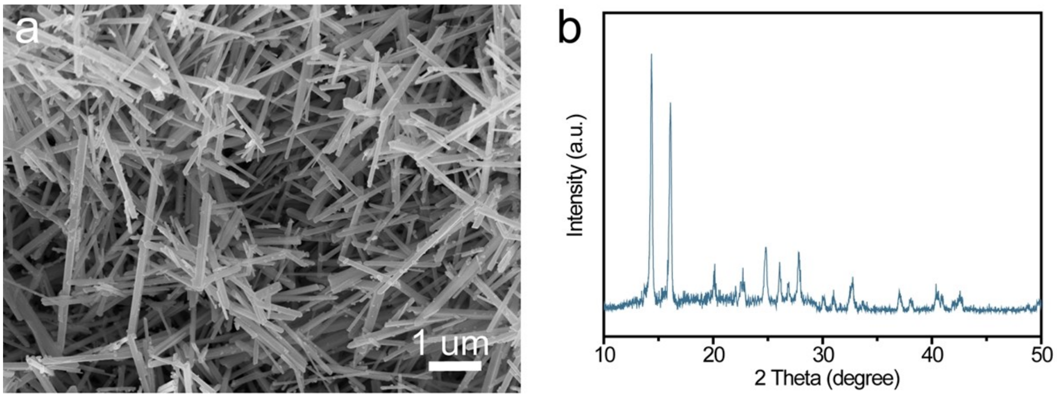

Fig. S12. (a) SEM image and (b) XRD pattern of Mn-TCNQ after stability test.

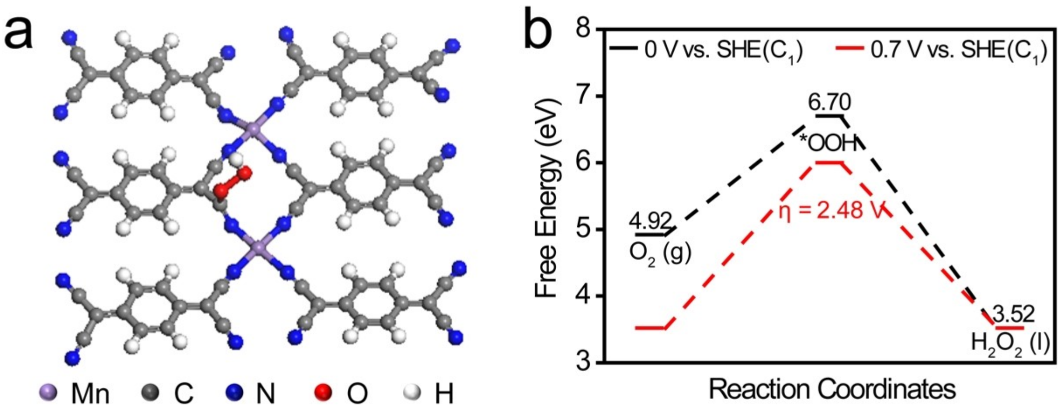

Fig. S13. (a) Atom configuration of C_1 sites attached to *OOH on Mn-TCNQ. (b) Free energy diagrams with the theoretical overpotentials (η) of the $2e^-$ ORR at the zero potential (black line) and the equilibrium potential (red line) for C_1 sites.

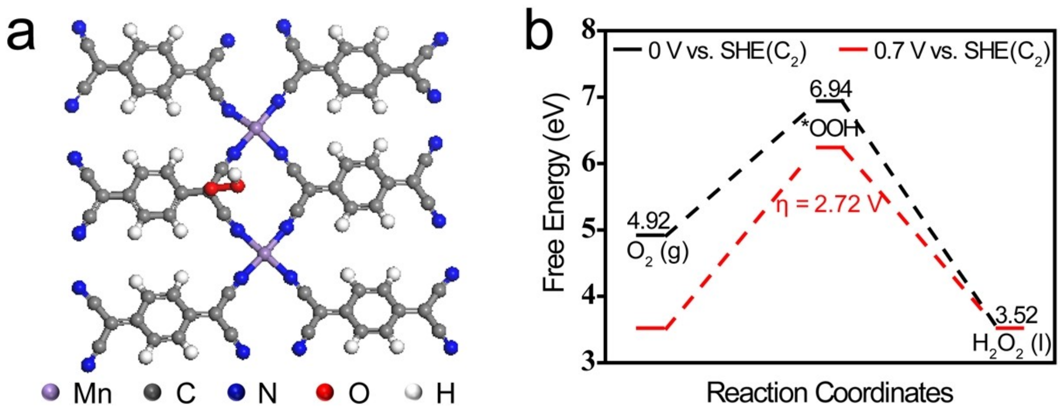

Fig. S14. (a) Atom configuration of C_2 sites attached to *OOH on Mn-TCNQ. (b) Free energy diagrams with the theoretical overpotentials (η) of the 2e⁻ ORR at the zero potential (black line) and the equilibrium potential (red line) for C_2 sites.

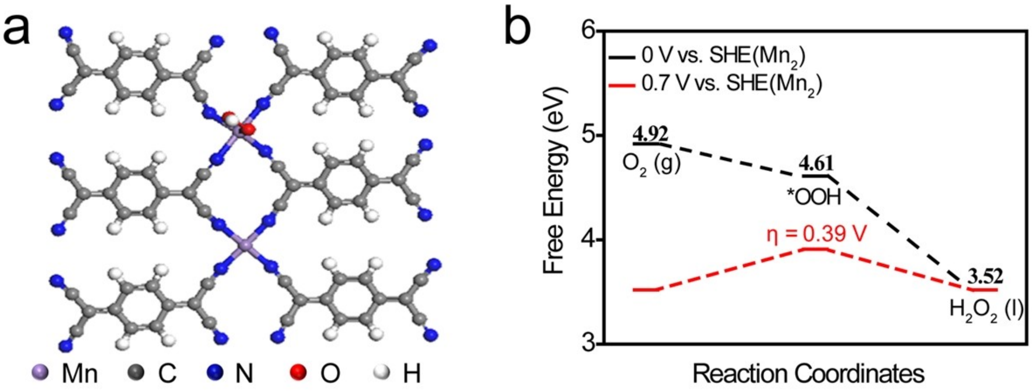

Fig. S15. (a) Atom configuration of Mn_2 sites attached to *OOH on Mn-TCNQ. (b) Free energy diagrams with the theoretical overpotentials (η) of the 2e⁻ ORR at the zero potential (black line) and the equilibrium potential (red line) for Mn_2 sites.

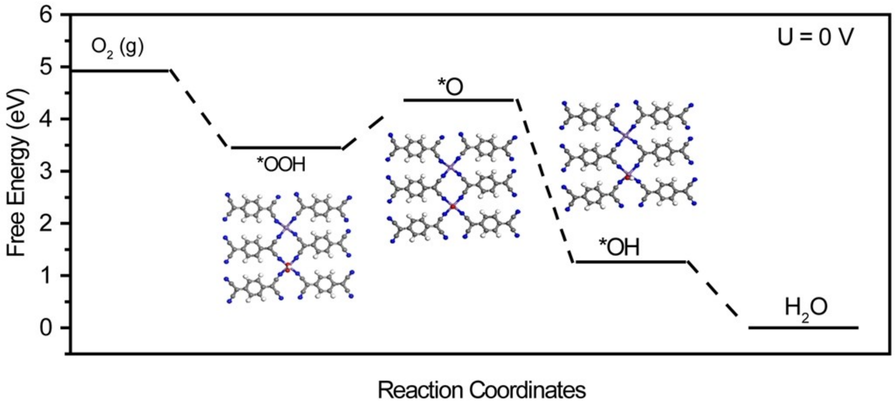

Fig. S16. Free energy diagrams of the 4e$^-$ ORR at the zero potential on Mn$_1$ sites for Mn-TCNQ.

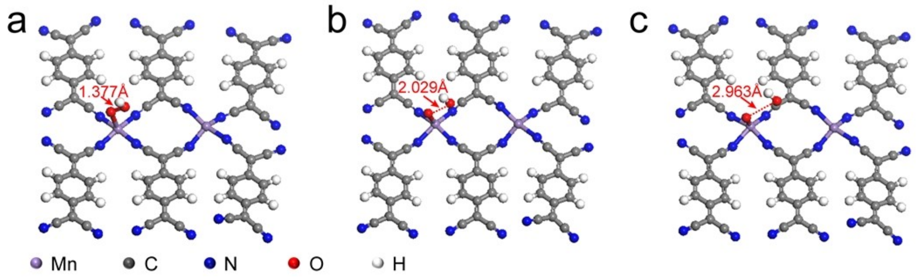

Fig. S17. The atom configurations of (a) initial, (b) transition and (c) final state for the chemical decomposition of *OOH to *OH.

Table S1.Peak positions of FTIR and Raman for TCNQ and Mn-TCNQ.

	C≡N		C=C ring		C=C wing		C-H	
	FTIR	Raman	FTIR	Raman	FTIR	Raman	FTIR	Raman
TCNQ	2223	2228	1545	1604	1354	1453	863	1209
Mn-TCNQ	2198	2243	1579/1507	1607	1321	1389	825	1213

Table S2. Comparison of Mn-TCNQ with reported 2e⁻ ORR catalysts for H_2O_2 production in alkaline solutions.

Catalyst	Selectivity (%@V vs. RHE)	Electrolyte	Stability	Overpotential (V vs. RHE)	Ref.
Zn-MOF	85@–0.6 V vs. Ag/AgCl	0.1 M KOH	/	/	5
Ni-N_2O_2/C	96@0.4	0.1 M KOH	8 h	/	6
NF-Cs	92.2@0.63	0.1 M KOH	6000 s	0.02	7
Mo SAC	95@0.4	0.1 M KOH	8 h	0	8
GOMC	95@0.7	0.1 M KOH	16 h	0	9
G-COF-950	75@0.5	0.1 M KOH	/	near-zero	10
Fe-MOF(550)	55.8@–0.5 V vs. Hg/HgO	0.1 M KOH	/	/	11
Fe-CNT	95@0.7	0.1 M KOH	8 h	0	12
Co-POC-O	85.6@0.78	0.1 M KOH	10 h	0	13
MOF NSs-300	99@0.45	0.1 M KOH	10 k cycles	near-zero	14
Ni_3B	90@0.5	0.1 M KOH	10 h	0.06	15
rGO-PEI	90.7@0.6	0.1 M KOH	3 h	/	16
CMK3-20s	91@0.7	0.1 M KOH	8 h	0	17
HPCS-S	70@0.4	0.1 M KOH	30000 s	0	18
Co_1-NG(O)	82@0.2	0.1 M KOH	110 h	0	19
N-FLG-8	95@0.3	0.1 M KOH	8 h	/	20
O-CNTs	90@0.4	0.1 M KOH	10 h	0.13	21
BN-C1	90@0.8	0.1 M KOH	50 h	0	22
Au-Pt-Ni NRs	95@0.5	0.1 M KOH	10 h	0.15	23
HCNFs	97.3@0.6	0.1 M KOH	12 h	0.01	24
Mn-TCNQ	**98.3@0.3**	**0.1 M KOH**	**24 h**	**0.01**	**This work**

Table S3. The bond lengths at C_1, C_2 and Mn sites after attached to *OOH.

Active sites	C-O/Mn-O (Å)	O-O (Å)
C_1	1.416	1.509
C_2	1.433	1.494
Mn	2.139	1.377

References

1 G. Kresse and J. Furthmüller, *Comp. Mater. Sci.*, 1996, **6**, 15−50.

2 G. Kresse and J. Furthmüller, *Phys. Rev. B*, 1996, **54**, 11169−11186.

3 J. P. Perdew, K. Burke and M. Ernzerhof, *Phys. Rev. Lett.*, 1996, **77**, 3865−3868.

4 S. Grimme, J. Antony, S. Ehrlich and H. Krieg, *J. Chem. Phys.*, 2010, **132**, 154104.

5 D. Das and V. Raut, *AIP Conf. Proc.*, 2019, **2115**, 030546.

6 Y. Wang, R. Shi, L. Shang, G. I. N. Waterhouse, J. Zhao, Q. Zhang, L. Gu and T. Zhang, *Angew. Chem. Int. Ed.,* 2020, **59**, 13057–13062.

7 N. Jia, T. Yang, S. Shi, X. Chen, Z. An, Y. Chen, S. Yin and P. Chen, *ACS Sustainable Chem. Eng.,* 2020, **8**, 2883−2891.

8 C. Tang, Y. Jiao, B. Shi, J.-N. Liu, Z. Xie, X. Chen, Q. Zhang and S.-Z. Qiao, *Angew. Chem. Int. Ed.,* 2020, **59**, 9171–9176.

9 Y. J. Sa, J. H. Kim and S. H. Joo, *Angew. Chem. Int. Ed.*, 2019, **131**, 1112−1117.

10 J. Zhang, G. Zhang, S. Jin, Y. Zhou, Q. Jia, H. Lan, H. Liu and J. Qu, *Carbon*, 2020, **163**, 154–161.

11 R. Liu, L. Ran, B. Niu and Y. Wei, *J. Nanosci. Nanotechnol.*, 2018, **18**, 4667–4674.

12 K. Jiang, S. Back, A. J. Akey, C. Xia, Y. Hu, W. Liang, D. Schaak, E. Stavitski, J. K. Nørskov, S. Siahrostami and H. Wang, *Nat. Commun.*, 2019, **10**, 3997.

13 B.-Q. Li, C.-X. Zhao, J.-N. Liu and Q. Zhang, *Adv. Mater.*, 2019, **31**, 1808173.

14 M. Wang, N. Zhang, Y. Feng, Z. Hu, Q. Shao and X. Huang, *Angew. Chem. Int. Ed.*, 2020, **59**, 14373−14377.

15 F. Ma, S. Wang, X. Liang, C. Wang, F. Tong, Z. Wang, P. Wang, Y. Liu, Y. Dai, Z. Zheng and B. Huang, *Appl. Catal. B-Environ.*, 2020, **279**, 119371.

16 X. Xiao, T. Wang, J. Bai, F. Li, T. Ma and Y. Chen, *ACS Appl. Mater. Interfaces*, 2018, **10**, 42534−42541.

17 Y.-L. Wang, S.-S. Li, X.-H. Yang, G.-Y. Xu, Z.-C. Zhu, P. Chen and S.-Q. Li, *J. Mater. Chem. A*, 2019, **7**, 21329−21337.

18 G. Chen, J. Liu, Q. Li, P. Guan, X. Yu, L. Xing, J. Zhang and R. Che, *Nano Res.*, 2019, **12**, 2614–2622.

19 E. Jung, H. Shin, B.-H. Lee, V. Efremov, S. Lee, H. S. Lee, J. Kim, W. H. Antink, S. Park, K.-S. Lee, S.-P. Cho, J. S. Yoo, Y.-E. Sung and T. Hyeon, *Nat. Mater., 2020*, **19**, 436–442.

20 L. Li, C. Tang, Y. Zheng, B. Xia, X. Zhou, H. Xu and S.-Z. Qiao, *Adv. Energy Mater.*, 2020, **10**, 2000789.

21 Z. Lu, G. Chen, S. Siahrostami, Z. Chen, K. Liu, J. Xie, L. Liao, T. Wu, D. Lin, Y. Liu, T. F. Jaramillo, J. K. Nørskov and Y. Cui, *Nat. Catal.*, 2018, **1**, 156–162.

22 S. Chen, Z. Chen, S. Siahrostami, D. Higgins, D. Nordlund, D. Sokaras, T. R. Kim, Y. Liu, X. Yan, E. Nilsson, R. Sinclair, J. K. Nørskov, T. F. Jaramillo and Z. Bao, *J. Am. Chem. Soc.*, 2018, **140**, 7851−7859.

23 Z. Zheng, Y. H. Ng, D.-W. Wang and R. Amal, *Adv. Mater.*, 2016, **28**, 9949–9955.

24 K. Dong, J. Liang, Y. Wang, Z. Xu, Q. Liu, Y. Luo, T. Li, L. Li, X. Shi, A. M. Asiri, Q. Li, D. Ma and X. Sun, *Angew. Chem. Int. Ed.*, 2021, **60**, 10583-10587.